Optica Applicata, Vol. XLVII, No. 2, 2017
DOI: 10.5277/oa170204

Digital volume correlation in an environment with intensive salt-and-pepper noise and strong monotonic nonlinear distortion of light intensity

PEIHAN TU[1], YULEI BAI[1], WEICHAO XU[1], BO DONG[1], SHUANGLI YE[2], QIYU YANG[1], YANZHOU ZHOU[1*]

[1]School of Automation, Guangdong University of Technology, Guangzhou, P.R. China, 510006

[2]School of Printing and Packaging, Wuhan University, Wuhan, P.R. China, 430072

[*]Corresponding author: zhouyanzhou@gdut.edu.cn

Digital volume correlation is an image-based technique for internal 3D displacement and strain fields measurement or analysis widely used in the field of experimental mechanics. A widely used correlation function (criterion) of digital volume correlation is Pearson correlation function, which suffers from the problem of the acquired data being contaminated by salt-and-pepper noise and monotonic nonlinear distortion of the light intensity. In this work, a 3D correlation function called the Spearman correlation function is used to deal with those interferences. A numerical experiment shows that the performance of Spearman correlation function using integer-pixel registration in an environment with 10% salt-and-pepper noise is better than that of Spearman and Pearson correlation functions using sub-pixel registration in an environment with 1% salt-and-pepper noise. As the light intensity distortion is significant, the error of Pearson correlation function is considerable; meanwhile, the error of Spearman correlation function is small. In conclusion, Spearman correlation function is, in particular, practical and useful in digital volume correlation.

Keywords: digital volume correlation, correlation function, salt-and-pepper noise, nonlinear effects.

1. Introduction

Digital volume correlation (DVC) is a technique that analyzes the 3D displacement field inside a structure. DVC has been widely used in experimental mechanics [1, 2, 3]. Since BAY introduced the DVC technique for volumetric strain measurement in 1999 [4], this measurement method has experienced a growth in technique and application [5]. SMITH *et al*. introduced the addition of rotational degrees of freedom into the minimization problem for DVC in order to improve the overall performance of the strain meas-

urement [6]. GATES *et al*. improved the DVC's accuracy using smoothing splines to address noisy image data [7]. In the same time, the computing speed of DVC algorithm has been improved a lot. In 2014, a 3D inverse compositional Gauss–Newton algorithm was introduced to replace the existing forward additive algorithms [8]. The experiment showed that the presented DVC algorithm produces a slightly higher accuracy at a substantially reduced computational cost. With the rapid development of parallel computing technology, GPU-based or CPU and GPU-based DVC method was proposed, which makes significant improvement in computation speed on common desktop computer [9, 10]. In 2015, a fast iterative digital volume correlation (FIDVC) method was presented, which can be run on a personal computer with computation times on the order of 1–2 min [11]. As much as application is concerned, DVC is useful to analyze complex materials, for example, bone [12, 13], rock [14], wood [15], sugar [16] and sand grains [17]. Furthermore, DVC can be used to analyze complicated mechanical properties of materials, such as material fatigue after repeated loading cycles [18, 19]. However, there is almost no literature about the improvement of DVC robustness in an environment with interference.

In 1D signal there is a typical additive interference called impulse noise, which exhibits a spiky pattern on rare occasions. The impulsive noise is often modeled with the so-called contaminated Gaussian model (CGM), whose probability density function (PDF) is expressed as a linear combination of two normal distributions. This type of noise can be caused by various factors such as electromagnetic interference (lightening), failures and/or faults in the system, and state changes of electrical components in the circuits. Similarly, in a digital speckle image, impulse noise is also present because of a quantum effect that is often called salt-and-pepper noise, which occurs sparsely in white and black pixels. In addition, salt-and-pepper (impulsive) noise is not rigidly defined. A lot of cases can be regarded as salt-and-pepper noise in broader terms, such as: dead pixel/voxel (bad point), and white pixel/voxel introduced by overexposure. Salt-and-pepper noise is so harmful to the digital imaging system that there are about seven hundred papers listed on Web of Science since 2000. Using a median filter is an effective noise reduction method. However, one of its disadvantages is that it significantly reduces the spatial resolution of the image. In a digital speckle image, in order to enhance the signal-to-noise ratio, local overexposure frequently exists. This results in a strong monotonic nonlinear effect on the intensity of the image, which is another fatal problem in digital correlation.

In the literature, many methods have been proposed and applied to quantify the intensity of correlation between two random variables. Among these methods, Pearson's product moment correlation coefficient (PPMCC) [20] and Spearman's rho (SR) [21] are the most widely used [22]. PPMCC is mainly used to characterize linear correlations, while SR is invariant under increasing monotone transformations. Thus, these methods are often considered as robust counterparts to the PPMCC [23, 24]. As shown in many theoretical and experimental results [25], the popular PPMCC, although optimal when the noise is Gaussian, is notoriously sensitive to impulsive noise that follows non-Gaussian distribution with a tail heavier than that of normal distribution [25].

On the other hand, SR has proven to be more robust for data corrupted by impulsive noise [25]. Motivated by the anti-nonlinearity and anti-impulsive noise features possessed by SR, we develop a novel DVC method based on SR in this work.

In the paper, a correlation study of the time-series signal system is extended into the digital volume imaging correlation for deformation evaluation, in an environment with a huge amount of salt-and-pepper noise and intensity change. The paper is organized as follows: Section 2 presents the definitions of DVC and SR and an analysis of SR's statistical properties, Section 3 discusses the numerical experiments, and Section 4 contains a discussion and conclusion.

2. Theory

2.1. Principle of DVC

DVC is a method that employs tracking and image registration techniques for the 3D evaluation of displacement, deformation, strain, *etc*., between the reference volumetric image and the deformed volumetric image, before and after an applied load. The subvolume $f(x, y, z)$ in the reference volumetric image, centered at the point (x_0, y_0, z_0), contains $(2M + 1) \times (2M + 1) \times (2M + 1)$ voxels (M is a positive integer). It is mapped to the optimal target subvolume $g(x', y', z')$ in the deformed volumetric image, centered at another point (x_0', y_0', z_0'), and contains $(2M + 1) \times (2M + 1) \times (2M + 1)$ voxels using DVC algorithm. The displacement components at (x_0, y_0, z_0) before and after displacement are $u(x_0, y_0, z_0) = x_0' - x_0$, $v(x_0, y_0, z_0) = y_0' - y_0$, and $w(x_0, y_0, z_0) = z_0' - z_0$ in the directions of x, y, and z, respectively.

Let $\{(X_i, Y_i)\}_{i=1}^{n}$ denote n independent and identically distributed (i.i.d.) data pairs drawn from a bivariate population with continuous joint distribution. Let $\overline{X}$ and $\overline{Y}$ be the mean of X_i and Y_i, respectively. The well-known Pearson's product moment correlation coefficient (PPMCC) is defined by

$$r_{\mathrm{P}} = \frac{\sum_{i=1}^{n}(X_i - \overline{X})(Y_i - \overline{Y})}{\sqrt{\sum_{i=1}^{n}(X_i - \overline{X})^2 \sum_{i=1}^{n}(Y_i - \overline{Y})^2}} \tag{1}$$

The correlation function, denoted by the Pearson correlation function (PCF), is essentially equal to zero-mean normalized cross-correlation (ZNCC) criterion in the sequel, which can be expressed as [1]

$$C_{\mathrm{P}}(u, v, w) = \frac{\sum \overline{f_i}\,\overline{g_i}}{\sqrt{\sum \overline{f_i}^2}\sqrt{\sum \overline{g_i}^2}} = C_{\mathrm{ZNCC}} \tag{2}$$

where f_i, g_i indicate the i-th pixels in f or g; $\overline{f}$ and $\overline{g}$ are the average values of the reference and target subvolumes, respectively, and $\overline{f_i} = f_i - \overline{f}$, $\overline{g_i} = g_i - \overline{g}$. It is well known that the PPMCC (and thus the PCF) is very sensitive to nonlinearity and

impulsive of salt-and-pepper noise. To address this problem, we employ a different correlation function that is robust against these kinds of interference.

2.2. Spearman correlation function and Gaussian model

2.2.1. Definition of Spearman correlation function

Let $\{(X_i, Y_i)\}_{i=1}^{n}$ denote n data pairs drawn from a bivariate population with continuous joint distribution. Sorting the X-variate in ascending order, we can get a new sequence $X_{(1)} < X_{(2)} < \ldots < X_{(n)}$. Assume that the element X_i is at k-th position in the sorted sequence. The number k is termed the rank of X_i and denoted by P_i. In a similar manner, we can also obtain the rank of Y_i which is denoted by Q_i. Then the rank-based correlation coefficient, Spearman's rho (SR), can be defined as [25]

$$r_S = 1 - \frac{6\sum_{i=1}^{n}(P_i - Q_i)^2}{n(n^2-1)} \tag{3}$$

From its definition above, it follows that SR depends only on the ranks, which are invariant under monotonic nonlinear transformations. Therefore, SR is robust against monotonic nonlinearities that might exist in the system.

Since a 3D image can be mapped to a 1D sequence, then $f(x, y, z)$ and $g(x+u, y+v, z+w)$ can be formulated as $(2M+1)^3$ data pairs, $\{(\Xi_i, Z_i)\}_{i=1}^{(2M+1)^3}$. Let P_i' and Q_i' be the ranks of Ξ_i and Z_i, respectively. Then the correlation function, named the Spearman correlation function (SCF), is

$$C_S(u, v, w) = 1 - \frac{6\sum_{i=1}^{(2M+1)^3}(P_i' - Q_i')^2}{(2M+1)^3\left[(2M+1)^6 - 1\right]} \tag{4}$$

Since the SCF is based on SR, it is also robust against monotonic nonlinearities. Moreover, as seen in Section 2.2.4, SCF is also robust against impulsive noise from the theoretical results [25].

2.2.2. Bivariate Gaussian model

In this work, the data pairs constructed from the original reference and deformed volumetric images are assumed to follow a bivariate Gaussian distribution with a probability density function (PDF):

$$\varphi(\xi, \zeta) = \frac{1}{2\pi\sigma_\Xi\sigma_Z\sqrt{1-\rho^2}}\exp\left[-\frac{z}{2(1-\rho^2)}\right] \tag{5}$$

where

$$z = \frac{\xi-\mu_\Xi}{\sigma_\Xi^2} - \frac{2\rho(\xi-\mu_\Xi)(\zeta-\mu_Z)}{\sigma_\Xi\sigma_Z} + \frac{\zeta-\mu_Z}{\sigma_Z^2} \tag{6}$$

and ρ is the parent correlation coefficient between Ξ and Z, μ is the mean value of the image, and σ^2 is the variances. For notational convenience, the bivariate Gaussian model of Eqs. (5) and (6) is abbreviated as

$$(\Xi, Z) \sim N(\mu_\Xi, \mu_Z, \sigma_\Xi^2, \sigma_Z^2, \rho) \tag{7}$$

2.2.3. Contaminated Gaussian model (CGM)

When the two original volumetric images are contaminated by salt-and-pepper noise with a large variance, we can employ the following contaminated Gaussian model to simulate this situation. Specifically, the PDF of the CGM can be expressed as

$$\begin{aligned} CN(\rho, \rho_1, \rho_2) \;=\; & (1-\varepsilon)N(\mu_\Xi, \mu_Z, \sigma_\Xi^2, \sigma_Z^2, \rho) \\ & + \frac{\varepsilon}{2}N(\mu_\Xi - \Delta\mu, \mu_Z - \Delta\mu, \sigma_{\Xi_1}^2, \sigma_{Z_1}^2, \rho_1) \\ & + \frac{\varepsilon}{2}N(\mu_\Xi + \Delta\mu, \mu_Z + \Delta\mu, \sigma_{\Xi_2}^2, \sigma_{Z_2}^2, \rho_2) \end{aligned} \tag{8}$$

where $0 \le \varepsilon \le 1$, $\Delta\mu \gg \mu_\Xi, \Delta\mu \gg \mu_Z, \sigma_{\Xi_1} \ll \sigma_\Xi, \sigma_{\Xi_2} \ll \sigma_\Xi, \sigma_{Z_1} \ll \sigma_Z, \sigma_{Z_2} \ll \sigma_Z, -1 \le \rho \le 1$; ρ_1 and ρ_2 are the population correlation coefficients with respect to the salt-and-pepper noise in the two volumetric images. The parameter ε, which is usually set to be small, represents the fraction of the salt-and-pepper noise contained in the images. Therefore, the first term in Eq. (8) corresponds to the joint distribution of the majority data pairs from the two images. With regard to the other two terms in Eq. (8), each one is a bivariate normal distribution tightly concentrated around locations far away from the center of majority, standing respectively for the joint distributions of the salt-and-pepper noise corrupting the two images.

2.2.4 Mean of PPMCC and SR under CGM

The mean of PPMCC under CGM (8) is

$$E(r_{\mathrm{P}}) \;=\; \frac{(1-\varepsilon)\sigma_\Xi\sigma_Z\rho + \varepsilon\Delta\mu^2}{\sqrt{\left[(1-\varepsilon)\sigma_\Xi^2 + \varepsilon\Delta\mu^2\right]\left[(1-\varepsilon)\sigma_Z^2 + \varepsilon\Delta\mu^2\right]}} \tag{9}$$

and when $\Delta\mu \to \infty$

$$E(r_{\mathrm{P}}) \approx 1 \tag{10}$$

Regardless of the dissimilarity between two uncontaminated subvolumes in an environment with salt-and-pepper noise, PPMCC always shows they are high correlated, as shown in Fig. 1. It suggests PPMCC cannot obtain a reliable value to evaluate the similarity between two subvolumes.

The mean of SR under CGM (8) is

$$E(r_{\mathrm{S}}) \;=\; \frac{6}{\pi}(1-3\varepsilon)\operatorname{asin}\left(\frac{\rho}{2}\right) + O(\varepsilon) \tag{11}$$

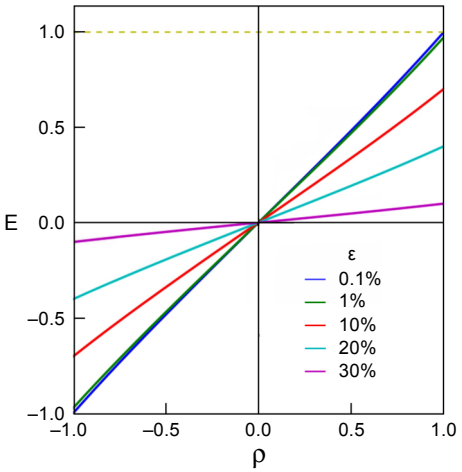

Fig. 1. Mean of PPMCC (dashed line) and SR (solid lines) under CGM. Blue, green, red, azure, and purple indicate the density of salt-and-pepper noise ε = 0.1%, 1%, 10%, 20%, 30%, respectively.

which, compared with the Eq. (10), suggests that there is a positive correlation between SR and ρ, as ε is relatively small, as shown in Fig. 1. This verifies the robustness of the proposed method against the salt-and-pepper noise in the DVC.

3. Numerical experiment

3.1. Generation of the volumetric image

In this work, there are two volumetric images, the reference and the deformed, each with a size of 200 × 200 × 200 voxels. In each volumetric image, there are 8000 speckle granules whose Gaussian distribution grayscales are of ellipsoid shapes. The radii of speckle granules are ranged between [2, 10]. The granule is rotated with angles between [–π/4, π/4]. The peak intensity is in the range [0.4, 1]. Volumetric images are generated by the superposition of all granules. The deformed volumetric image is of a linear compression of the reference volumetric image in the directions z, and linear compression rate is 0.95.

In the end, both original reference $F_o(x, y, z)$ and target image $G_o(x, y, z)$ are normalized to the range [0, 0.7].

In order to verify the robustness of the SCF in an environment with salt-and-pepper noise and monotonic light intensity distortion, the contaminated volumetric images $F(x, y, z)$ and $G(x, y, z)$ are defined as

$$F(x,y,z) = \begin{cases} 0 & \text{with probability } \varepsilon/2 \\ 1 & \text{with probability } \varepsilon/2 \\ F_o(x,y,z) + n_1(x,y,z) & \text{with probability } (1-\varepsilon) \end{cases} \tag{12a}$$

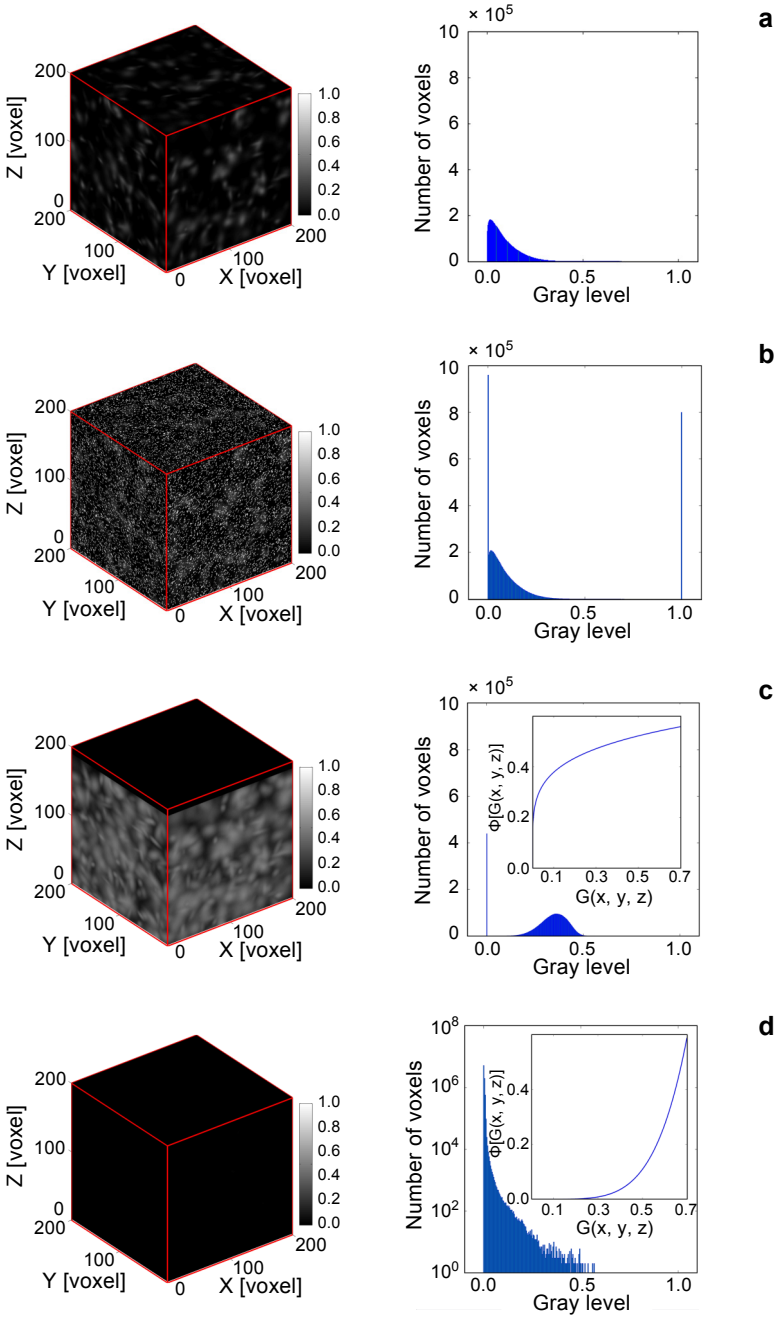

Fig. 2. Volumetric images and their histograms. Original reference volumetric image (**a**), reference volumetric image contaminated by $\varepsilon = 20\%$ salt-and-pepper noise only (**b**), deformed volumetric image with concave distortion of light intensity $\Phi[G_o(x, y, z)] = 0.6[G_o(x, y, z)]^{1/5}$ only (**c**), deformed volumetric image with convex distortion of light intensity $\Phi[G_o(x, y, z)] = 3.5[G_o(x, y, z)]^5$ only (**d**).

$$G(x, y, z) = \begin{cases} 0 & \text{with probability } \varepsilon/2 \\ 1 & \text{with probability } \varepsilon/2 \\ \Phi[G_o(x, y, z)] + n_2(x, y, z) & \text{with probability } (1 - \varepsilon) \end{cases} \quad (12b)$$

where $n_1(x, y, z)$ and $n_2(x, y, z)$ are Gaussian noise with mean μ_G and variance σ_G^2 in the reference and deformed volumetric images, respectively; $\Phi(\cdot)$ is the function of monotonic light intensity distortion. Figures 2**a** and 2**b** show the original reference volumetric image without interference and contaminated by $\varepsilon = 20\%$ salt-and-pepper noise only, respectively. Figures 2**c** and 2**d** show the deformed volumetric images with concave and convex distortions of the light intensity $\Phi[G_o(x, y, z)] = 0.6[G_o(x, y, z)]^{1/5}$ and $\Phi[G_o(x, y, z)] = 3.5[G_o(x, y, z)]^5$ without noise, respectively.

3.2 Numerical experiment and results

3.2.1. Searching scheme

In this work, $m = (10 \times 10 \times 10)$ regularly distributed points in the volumetric images are chosen as the centers of the subvolumes, respectively. The size of each subvolume is $(15 \times 15 \times 15)$ voxels. The central distance between neighboring subvolumes is 20 voxels. Each subvolume in the reference volumetric image is processed to map the most optimal subvolume in the deformed volumetric image at a range of 20 voxels in the directions x, y, and z, respectively, using simple integer voxel displacement searching. In the end, the displacement of the center of the i-th subvolume $l^i_{x,y,z}$ is achieved in one direction, respectively, where the subscript c represents the results of the correlation searching. If the displacement of the i-th subvolume is presented as $L^i_{x,y,z}$, the mean absolute error $\overline{d}_{x,y,z}$ and standard deviation error $\sigma_{x,y,z}$, are defined as

$$\begin{aligned} \overline{d}_{x,y,z} &= \frac{1}{m}\sum_{i=1}^{m}\sqrt{(l^i_{x,y,z} - L^i_{x,y,z})^2} \\ \sigma_{x,y,z} &= \sqrt{\frac{1}{m-1}\sum_{i=1}^{m}\left[(l^i_{x,y,z} - L^i_{x,y,z}) - \frac{1}{m}\sum_{i=1}^{m}(l^i_{x,y,z} - L^i_{x,y,z})\right]^2} \end{aligned} \quad (13)$$

3.2.2. PCF and SCF with Gaussian noise

Suppose that there is Gaussian noise $[\mu_G, \sigma_G] = (0, 0.008)$ only in the volumetric images. Table 1 shows the mean absolute and standard deviation errors of PCF and SCF

T a b l e 1. Mean absolute and standard deviation errors of PCF and SCF using simple integer voxel displacement searching $[\mu_G, \sigma_G] = (0, 0.008)$; unit: voxel.

	$\overline{d}_x$	$\overline{d}_y$	$\overline{d}_z$	σ_x	σ_y	σ_z
PCF	0.012	0.005	0.508	0.095	0.048	0.476
SCF	0.015	0.008	0.523	0.112	0.088	0.485

using simple integer voxel displacement searching, respectively. PCF is more robust than SCF in an environment with Gaussian noise. This conforms to the theory in [21]. However, it is noted that there are no significant differences in their application, because these computing errors between SCF and PCF are within the range of 0.05 pixels.

3.2.3. PCF and SCF in an environment with salt-and-pepper noise

The robustness of PCF and SCF in an environment with salt-and-pepper noise and Gaussian noise $[\mu_G, \sigma_G] = (0, 0.008)$ is investigated first. If $F(x, y, z)$ and $G(x, y, z)$ are contaminated with salt-and-pepper noise $\varepsilon = 1\%$, the displacement fields evaluated by PCF are shown in Fig. 3**a** in the directions x, y, and z, respectively. Those displacement fields produce irregular distributed errors, which are more than 10 voxels in some places. Therefore, it is concluded that PCF is invalid as $\varepsilon > 1\%$. Meanwhile, the displacement error of SCF is so small that it is ignored in the text for simplicity. As $F(x, y, z)$ and $G(x, y, z)$ are contaminated by the salt-and-pepper noise with a density of 1% and

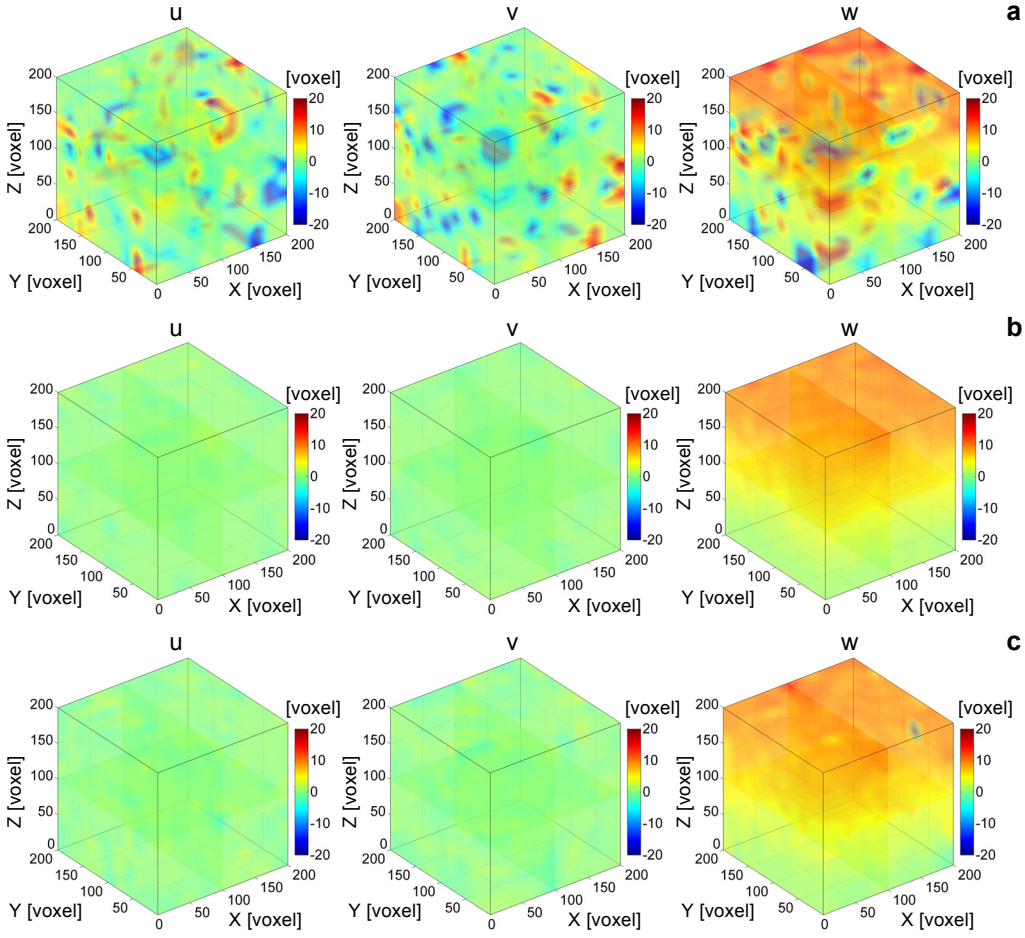

Fig. 3. Continued on the next page.

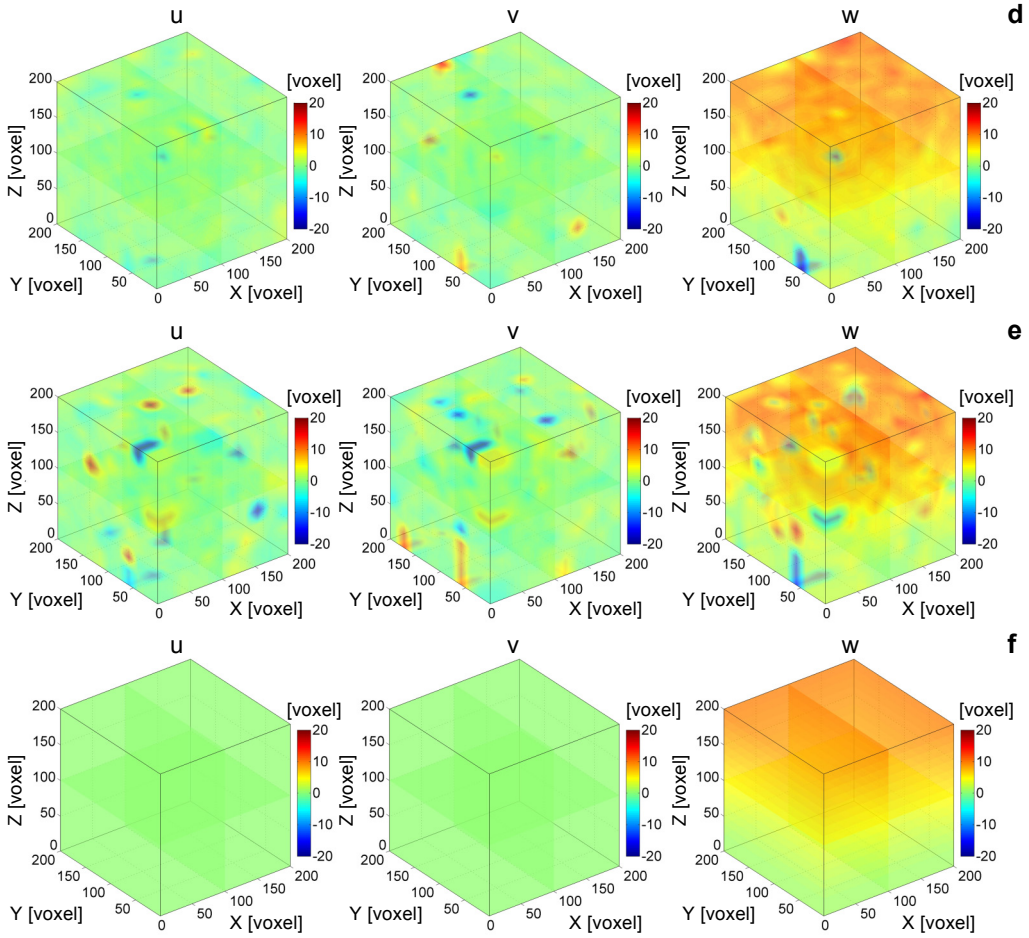

Fig. 3. Distributions of displacement field using simple integer voxel displacement searching in directions x, y, and z, respectively. PCF, ε = 1%, [μ_G, σ_G] = (0, 0.008) (**a**), SCF, ε = 10%, 20%, 30%, and 40%, respectively, as [μ_G, σ_G] = (0, 0.008) (**b**–**e**), and reference displacement field (**f**).

from 10% to 40%, the displacement field distributions using SCF are shown in Figs. 3**b** to 3**e**, respectively. The robustness of SCF is so good that its errors, even though ε = 40%, [μ_G, σ_G] = (0, 0.008), are less than those of PCF as ε = 1%, [μ_G, σ_G] = (0, 0.008). Figure 3**f** shows the reference displacement field without salt-and-pepper noise. Its mean absolute and standard deviation errors are still smaller than those of PCF as ε = 1%, and [μ_G, σ_G] = (0, 0.008), as shown in Fig. 4. Therefore, it is concluded that the errors of DVC are mainly a result of the salt-and-pepper noise rather than the Gaussian noise. In this case, SCF is the best solution.

Figure 4 shows the mean absolute and standard deviation errors of the displacement field using PCF and SCF with ε = 1%, 10%, 20%, 30%, and 40%, respectively. Those

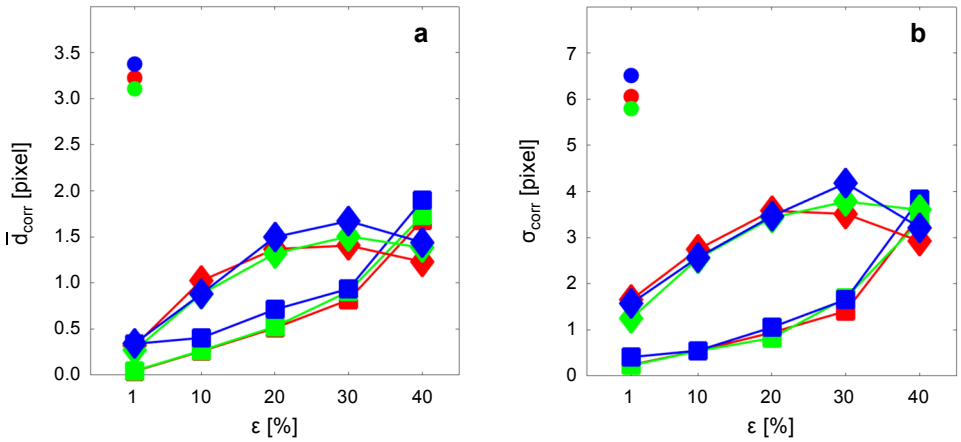

Fig. 4. Errors of displacement field in environment with salt-and-pepper noise. Mean absolute error (**a**), and standard deviation error (**b**) (red, green, and blue represent the directions x, y, and z, respectively). ● – PCF using simple integer voxel displacement searching, $[\mu_G, \sigma_G] = (0, 0.008)$, ■ – SCF using simple integer voxel displacement searching, $[\mu_G, \sigma_G] = (0, 0.008)$, and ◆ – SCF using curve-fitting, $[\mu_G, \sigma_G] = (0, 0.008)$.

errors in all directions x, y, and z are approximately equal to each other. When $\varepsilon = 1\%$, the mean absolute and standard deviation errors in the directions x, y, and z using PCF are more than 3 and 5.5 voxels, respectively. When $\varepsilon = 40\%$, the mean absolute and standard deviation errors in the directions x, y, and z using SCF are less than 2 and 4 voxels, respectively. The errors of PCF when $\varepsilon = 1\%$ are larger than those of SCF when $\varepsilon = 40\%$.

3.2.4. PCF and SCF in an environment with monotonic nonlinear distortion of light intensity

To verify the robustness of SCF in an environment with nonlinear distortion of light intensity with $\Phi[G_o(x, y, z)] = 3.5[G_o(x, y, z)]^5$ and $\Phi[G_o(x, y, z)] = 0.6[G_o(x, y, z)]^{1/5}$, respectively, the density of the salt-and-pepper noise ε is set to be 0 and the Gaussian noise is set to be $[\mu_G, \sigma_G] = (0, 0.008)$. Table 2 shows the mean absolute and standard deviation errors using PCF and SCF, respectively. PCF is not as robust as SCF when a significant nonlinear distortion of the light intensity exists. It is noted that the per-

T a b l e 2. Mean absolute and standard deviation errors using simple integer voxel displacement searching in environment with nonlinear distortion of light intensity with Gaussian noise of $[\mu_G, \sigma_G] = (0, 0.008)$; unit: voxel.

	Light intensity distortion	$\bar{d}_x$	$\bar{d}_y$	$\bar{d}_z$	σ_x	σ_y	σ_z
PCF	$\Phi[G_o(x, y, z)] = 3.5[G_o(x, y, z)]^5$	2.677	2.676	2.701	5.623	5.672	5.758
	$\Phi[G_o(x, y, z)] = 0.6[G_o(x, y, z)]^{1/5}$	0.269	0.280	0.473	1.299	1.222	1.603
SCF	$\Phi[G_o(x, y, z)] = 3.5[G_o(x, y, z)]^5$	0.097	0.116	0.499	0.380	0.626	0.567
	$\Phi[G_o(x, y, z)] = 0.6[G_o(x, y, z)]^{1/5}$	0.089	0.111	0.506	0.411	0.620	0.578

formances of both PCF and SCF are acceptable in the case where the light intensity distortion is not severe.

3.2.5. Sub-voxel registration using PCF and SCF

In general, higher accuracy can be obtained by a using sub-voxel registration algorithm. To verify the robustness of SCF and morbidity of PCF, two kinds of sub-voxel registration algorithms, in an environment with salt-and-pepper noise and nonlinear distortion, are employed [26] with manually set initial guess: *i*) PCF using Newton–Raphson method; *ii*) SCF using correlation coefficient curve-fitting method.

Environment with salt-and-pepper noise. Though initial guess is accurate, PCF using sub-voxel registration is easily affected by salt-and-pepper noise. Its errors ($\varepsilon = 0.2\%$, $\sigma_z = 0.235$) increase rapidly as $\varepsilon < 0.2\%$. As $\varepsilon \geq 0.2\%$, the errors do not increase with ε anymore, because the results are totally uncorrelated with the intensity information of the reference and target images, according to Eq. (8). Meanwhile, the errors of SCF ($\varepsilon = 1\%$, $\sigma_z = 0.169$) increase slowly as $\varepsilon < 1\%$. As $\varepsilon > 1\%$, they increase rapidly due to miscalculations of curve-fitting. In a word, as $\varepsilon > 1\%$, both PCF and SCF are invalid. As shown in Fig. 4, the error of SCF using sub-pixel registration is larger than that using simple integer voxel displacement searching, $\varepsilon > 1\%$. Therefore, it is concluded that SCF using integer-pixel registration algorithm is the only efficacious algorithm when there is salt-and-pepper noise in the volume image.

T a b l e 3. Mean absolute and standard deviation errors using sub-voxel registration in environment with nonlinear distortion of light intensity with Gaussian noise of $[\mu_G, \sigma_G] = (0, 0.008)$; unit: voxel.

	Light intensity distortion	$\overline{d}_x$	$\overline{d}_y$	$\overline{d}_z$	σ_x	σ_y	σ_z
PCF	$\Phi[G_o(x, y, z)] = 3.5[G_o(x, y, z)]^5$	0.361	0.395	0.405	0.498	0.445	0.545
	$\Phi[G_o(x, y, z)] = 0.6[G_o(x, y, z)]^{1/5}$	0.063	0.079	0.093	0.081	0.104	0.075
SCF	$\Phi[G_o(x, y, z)] = 3.5[G_o(x, y, z)]^5$	0.031	0.029	0.016	0.038	0.037	0.043
	$\Phi[G_o(x, y, z)] = 0.6[G_o(x, y, z)]^{1/5}$	0.033	0.032	0.028	0.049	0.044	0.044

Environment with nonlinear light intensity distortion. Different from PCF, SCF is less affected by nonlinear light intensity distortion, shown in Table 3. The mean absolute error and standard deviation of PCF increase a lot as nonlinear light intensity distortion exists.

4. Conclusions and discussion

Recently, DVC has experienced rapid development in 3D mechanical strain analysis. However, the algorithm based on PCF is sensitive to salt-and-pepper noise and nonlinear distortion of light intensity. In terms of research on the statistical characteristics of the correlation coefficients for the time signal process, this work proposes a DVC algorithm based on SCF that utilizes the robustness of SR in an environment with impulsive noise and monotonic nonlinear distortion to process the 3D data.

The performance of SCF using a simple integer voxel displacement searching as $\varepsilon = 40\%$ is better than that of PCF as $\varepsilon = 1\%$. PCF using sub-voxel registration as $\varepsilon > 0.2\%$, and SCF using sub-voxel registration as $\varepsilon > 1\%$ leads to large errors. In general, sub-voxel registration is invalid as there is salt-and-pepper noise in the volumetric images, while integer-pixel registration is still robust as the concentration of salt-and -pepper noise is about 10%–20%. In an environment with nonlinear light intensity distortion, SCF using integer-pixel registration and sub-voxel registration are relatively robust, while PCF using integer-pixel registration is morbid.

It is noted that there are several other correlation criteria [27]; 1) the zero-mean normalized sum of absolute difference (ZNSAD), 2) the zero-mean normalized sum of squared difference (ZNSSD), and 3) the parametric sum of the squared difference (PSSD). Bing Pan *et al*. have proved that the performances of C_{PSSDab} and C_{ZNSSD} are approximately equivalent to C_{ZNCC} [27], which is PCF in essence. These four correlation criteria are to evaluate the similarity between the reference and target subsets, in terms of the information of gray level. In environment with Gaussian noise, the robustness of C_{ZNCC} is the best. However, they are not robust in an environment with either salt -and-pepper noise or nonlinearity intensity distortion.

In this paper, Newton–Raphson method is employed as the sub-voxel registration algorithm based on PCF, which has been widely used [26]. Due to the discontinuity of SCF, it cannot be optimized by Newton–Raphson. Therefore, curve-fitting method is used as a sub-voxel registration algorithm for SCF in this paper. A new sub-voxel registration is desirable for SCF, which should be able to enhance the accuracy in an environment with high concentrations of salt-and-pepper noise.

Although SCF is a promising criterion for DVC/DIC, there are many problems which should be addressed in the future. First of all, SCF is better served as a correlation criterion of DVC in an environment with salt-and-pepper noise or nonlinear light intensity distortion. However, its computation efficiency is low. The usage of parallel computing technology can improve its efficiency. Furthermore, new algorithms combining SCF and warp functions should be developed in the future.

Because salt-and-pepper noise and the nonlinear monotonic effect of light intensity are common interferences in confocal microscopy, μCT, *etc*., it is concluded that the application of SCF in DVC is very helpful and practical in mechanical analysis.

Acknowledgements – The authors wish to thank the Science and Technology Project of Guangdong Province (STPGP) (2016A020220017), Natural Science Foundation of Guangdong Province (NSFGP) (2014A030313519).

References

[1] Leclerc H., Périé J.-N., Roux S., Hild F., *Voxel-scale digital volume correlation*, Experimental Mechanics **51**(4), 2011, pp. 479–490.

[2] Fedele R., Ciani A., Fiori F., *X -ray microtomography under loading and 3D-volume digital image correlation. A review*, Fundamenta Informaticae **135**(1–2), 2014, pp. 171–197.

[3] BING PAN, DAFANG WU, ZHAOYANG WANG, *Internal displacement and strain measurement using digital volume correlation: a least-squares framework*, Measurement Science and Technology **23**(4), 2012, article ID 045002.
[4] BAY B.K., SMITH T.S., FYHRIE D.P., SAAD M., *Digital volume correlation: three-dimensional strain mapping using X-ray tomography*, Experimental Mechanics **39**(3), 1999, pp. 217–226.
[5] BAY B.K., *Methods and applications of digital volume correlation*, Journal of Strain Analysis for Engineering Design **43**(8), 2008, pp. 745–760.
[6] SMITH T.S., BAY B.K., RASHID M.M., *Digital volume correlation including rotational degrees of freedom during minimization*, Experimental Mechanics **42**(3), 2002, pp. 272–278.
[7] GATES M., LAMBROS J., HEATH M.T., *Towards high performance digital volume correlation*, Experimental Mechanics **51**(4), 2011, pp. 491–507.
[8] BING PAN, BO WANG, DAFANG WU, LUBINEAU G., *An efficient and accurate 3D displacements tracking strategy for digital volume correlation*, Optics and Lasers in Engineering **58**, 2014, pp. 126–135.
[9] WANG T., JIANG Z., KEMAO Q., LIN F., SOON S.H., *GPU accelerated digital volume correlation*, Experimental Mechanics **56**(2), 2016, pp. 297–309.
[10] GATES M., HEATH M.T., LAMBROS J., *High-performance hybrid CPU and GPU parallel algorithm for digital volume correlation*, International Journal of High Performance Computing Applications **29**(1), 2015, pp. 92–106.
[11] BAR-KOCHBA E., TOYJANOVA J., ANDREWS E., KIM K.-S., FRANCK C., *A fast iterative digital volume correlation algorithm for large deformations*, Experimental Mechanics **55**(1), 2015, pp. 261–274.
[12] LI LIU, MORGAN E.F., *Accuracy and precision of digital volume correlation in quantifying displacements and strains in trabecular bone*, Journal of Biomechanics **40**(15), 2007, pp. 3516–3520.
[13] ZAUEL R., YENI Y.N., BAY B.K., DONG X.N., FYHRIE D.P., *Comparison of the linear finite element prediction of deformation and strain of human cancellous bone to 3D digital volume correlation measurements*, Journal of Biomechanical Engineering **128**(1), 2006, pp. 1–6.
[14] LENOIR N., BORNERT M., DESRUES J., BÉSUELLE P., VIGGIANI G., *Volumetric digital image correlation applied to X-ray microtomography images from triaxial compression tests on argillaceous rock*, Strain **43**(3), 2007, pp. 193–205.
[15] FORSBERG F., SJÖDAHL M., MOOSER R., HACK E., WYSS P., *Full three-dimensional strain measurements on wood exposed to three-point bending: analysis by use of digital volume correlation applied to synchrotron radiation microcomputed tomography image data*, Strain **46**(1), 2010, pp. 47–60.
[16] FORSBERG F., SIVIOUR C.R., *3D deformation and strain analysis in compacted sugar using X-ray microtomography and digital volume correlation*, Measurement Science and Technology **20**(9), 2009, article ID 095703.
[17] HALL S.A., BORNERT M., DESRUES J., PANNIER Y., LENOIR N., VIGGIANI G., BÉSUELLE P., *Discrete and continuum analysis of localised deformation in sand using X-ray μCT and volumetric digital image correlation*, Géotechnique **60**(5), 2010, pp. 315–322.
[18] RANNOU J., LIMODIN N., RÉTHORÉ J., GRAVOUIL A., LUDWIG W., BAÏETTO-DUBOURG M.-C., BUFFIÈRE J.-Y., COMBESCURE A., HILD F., ROUX S., *Three dimensional experimental and numerical multiscale analysis of a fatigue crack*, Computer Methods in Applied Mechanics and Engineering **199**(21–22), 2010, pp. 1307–1325.
[19] CARROLL J., EFSTATHIOU C., LAMBROS J., SEHITOGLU H., HAUBER B., SPOTTSWOOD S., CHONA R., *Investigation of fatigue crack closure using multiscale image correlation experiments*, Engineering Fracture Mechanics **76**(15), 2009, pp. 2384–2398.
[20] FISHER R.A., *On the 'probable error' of a coefficient of correlation deduced from a small sample*, Metron **1**, 1921, pp. 3–32.
[21] KENDALL M., GIBBONS J.D., *Rank Correlation Methods*, 5th Edition, Oxford University Press, New York, 1990.
[22] MARI D.D., KOTZ S., *Correlation and Dependence*, Imperial College Press, London, 2001.

[23] Weichao Xu, Chunqi Chang, Hung Y.S., Kwan S.K., Peter Chin Wan Fung, *Order statistics correlation coefficient as a novel association measurement with applications to biosignal analysis*, IEEE Transactions on Signal Processing **55**(12), 2007, pp. 5552–5563.

[24] Weichao Xu, Chunqi Chang, Hung Y.S., Peter Chin Wan Fung, *Asymptotic properties of order statistics correlation coefficient in the normal cases*, IEEE Transactions on Signal Processing **56**(6), 2008, pp. 2239–2248.

[25] Weichao Xu, Yunhe Hou, Hung Y.S., Yuexian Zou, *A comparative analysis of Spearman's rho and Kendall's tau in normal and contaminated normal models*, Signal Processing **93**(1), 2013, pp. 261–276.

[26] Pan Bing, Xie Hui-min, Xu Bo-qin, Dai Fu-long, *Performance of sub-pixel registration algorithms in digital image correlation*, Measurement Science and Technology **17**(6), 2006, pp. 1615–1621.

[27] Bing Pan, Huimin Xie, Zhaoyang Wang, *Equivalence of digital image correlation criteria for pattern matching*, Applied Optics **49**(28), 2010, pp. 5501–5509.

Received March 25, 2016
in revised form August 14, 2016